Low Mach number slip flow through diverging microchannel

CrossMark

Vijay Varade [a], V.S. Duryodhan [b], Amit Agrawal [b,*], A.M. Pradeep [c], Amin Ebrahimi [d], Ehsan Roohi [d]

[a] Centre for Research in Nanotechnology and Science, Indian Institute of Technology Bombay, 400076, India
[b] Department of Mechanical Engineering, Indian Institute of Technology Bombay, Mumbai 400076, India
[c] Department of Aerospace Engineering, Indian Institute of Technology Bombay, Mumbai 400076, India
[d] High Performance Computing (HPC) Laboratory, Department of Mechanical Engineering, Ferdowsi University of Mashhad, P.O. Box: 91775-1111, Mashhad, Iran

ARTICLE INFO

ABSTRACT

This paper presents experimental and three-dimensional numerical study of gaseous slip flow through diverging microchannel. The measurements are performed for nitrogen gas flowing through microchannel with different divergence angles ($4°$, $8°$, $12°$ and $16°$), hydraulic diameters (118, 147 and 177 μm) and lengths (10, 20 and 30 mm). The Knudsen number falls in the continuum and slip regimes ($0.0005 \leqslant Kn \leqslant 0.1$; Mach number is between 0.03 and 0.2 for the slip regime) while the flow Reynolds number ranges between 0.4 and 1280. The static pressure drop is measured for various mass flow rates; and it is observed that the pressure drop decreases with an increase in the divergence angle. The viscous component has a relatively large contribution in the overall pressure drop. The numerical solution of the Navier–Stokes equations with the Maxwell's slip boundary condition shows absence of flow reversal (due to slip at the wall), larger viscous diffusion and lower kinetic energy in the diverging microchannel. The centerline velocity and wall shear stress decrease with an increase in the divergence angle. The numerical results further show three different flow behaviors: a nonlinear pressure variation with rapid flow deceleration in the initial part of the microchannel; uniform centerline velocity with linear pressure variation in the middle part, and flow acceleration with nonlinear pressure variation in the last part of the microchannel. A characteristic length scale for diverging microchannel is also defined. The location of the characteristic length is a function of the Knudsen number and shifts toward the microchannel inlet with rarefaction. Mass flow rate and pressure distribution along the channel are also obtained numerically from the direct simulation Monte Carlo (DSMC) method and compared suitably with the experimental data or Navier–Stokes solutions. Empirical relations for the mass flow rate and Poiseuille number are suggested. These results on gaseous slip flow through diverging microchannels are considerably different than their continuum counterparts, and are not previously available.

1. Introduction

Expansion, which may be sudden or gradual, appears fundamental to micro-systems such as microactuators, microturbines, gas chromatographs, and micro air vehicles. Therefore, study of rarefied gas flow through diverging microchannel is important for both engineering and scientific applications. It is important to understand the gas flow behavior through such geometry in terms of pressure drop, velocity distribution and flow structure. Most of the earlier work however focused on uniform cross-section microchannels with liquid or gas flow [1–12] and flow through other cross-section area microchannels have been inadequately studied. The low pressure gas flows through conventional tubes are governed by the same set of non-dimensional parameters as that of gas microflow; Sreekanth [13] and Demsis et al. [14,15]. A comprehensive review on gas flow in microchannel was reported by Agrawal [16].

Relatively few studies explore *incompressible* flow through microchannel with expansion. Pan et al. [17] observed flow separation at the junction for liquid flow through a microchannel with a sudden expansion. Similarly, the experimental study on liquid flow by Tsai et al. [18] indicated formation of a separation vortex at the sudden expansion corner of a high aspect ratio microchannel. Duryodhan et al. [19] inferred that flow separation occurs in a diverging microchannel with water flow beyond a critical divergence angle of $16°$; the critical value of divergence angle agrees with the corresponding value for continuum flow. Abdelall et al. [20] experimentally investigated the pressure drop caused by flow of

* Corresponding author. Tel.: +91 22 2576 7516.
E-mail addresses: vijvarade@yahoo.co.in (V. Varade), vijud25@gmail.com (V.S. Duryodhan), amit.agrawal@iitb.ac.in (A. Agrawal), ampradeep@aero.iitb.ac.in (A.M. Pradeep), ebrahimi.amin@gmail.com (A. Ebrahimi), e.roohi@um.ac.ir (E. Roohi).

(continuum) air and water through sudden expansion in a microtube (1000 < *Re* < 7000). They reported that the expansion and contraction loss coefficients are different for air and water flows. The above studies indicate that flow separation occurs with liquid flow through microchannel with sudden/gradual expansion.

Study of liquid flow through diverging/converging sections has also been undertaken in the context of micro-pump by Stemme and Stemme [21], Olson et al. [22], Gerlach [23], Singhal et al. [24] and Wang et al. [25]. Akbari et al. [26] studied liquid flow through a series of diverging microchannels and proposed an analytical model for calculating the flow resistance.

The behavior of *rarefied gas flow* is however different than that of the liquid flow as reviewed next. Rathakrishnan and Sreekanth [27] studied rarefied gas flow (*Kn* = 0.0026–1.75, Nitrogen) through circular tube with sudden increase in cross sectional area. They noted that in the transition regime, the pressure ratio and length to diameter ratio of the passage strongly influence the discharge through sudden enlargements. In a recent experimental study involving flow through a sudden expansion, Varade et al. [28] observed a discontinuity in the slope of pressure and absence of flow separation at the junction; in the slip regime. These measurements are qualitatively similar to the two-dimensional planar simulations of Agrawal et al. [29]. Lee et al. [30] in an experimental study on gas flow through microchannels connected through diverging section observed that the mass flow rate decreases and the pressure loss increases with increasing included angle of the transition section.

It can be noted that a systematic and detailed analysis for rarefied gas flow through diverging microchannels is not available. Further, there is ambiguity in the literature about the characteristic dimension to be employed for obtaining non-dimensional parameters [21,23,31]. These issues provided the motivation for undertaking the current work. The objectives of this work are to investigate the gas flow behavior through a diverging microchannel and to highlight significant differences with respect to continuum flow behavior. The static pressure drop is measured for different mass flow rates and analyzed in this work. The numerical simulations are performed to obtain the local variation in flow parameters for gaseous slip flow through diverging microchannel.

2. Measurement system

2.1. Experimental facility

The experimental facility is similar to that employed by Varade et al. [28,45,46]. It consists of a vacuum system, inlet reservoir, outlet reservoir and mass flow controller as shown in Fig. 1a. The vacuum system consists of a diffusion pump (maximum pumping speed of 700 lpm, 1.31×10^{-2} kg/s) and a rotary pump (speed of 350 lpm, 6.55×10^{-3} kg/s). The lowest absolute pressure that can be accomplished by the vacuum system is 10^{-4} Pa. An air filter is mounted in the incoming gas stream for blocking particles (particle size > 25 µm). The different Reynolds and Knudsen numbers are attained by using two different mass flow controllers (M/s MKS Instruments, range 0–20 and 0–200 sccm or standard cubic centimeters per minute). The absolute pressure at the test section is measured by two absolute pressure transducers (also from M/s MKS Instruments, range 0–10,000 or 0–100,000 Pa). The uncertainty in measurement of flow rate and pressure along with other measured and derived parameters is provided in Table 1.

2.2. Diverging microchannel

The diverging microchannel with trapezoidal cross section geometry is shown in Fig. 1b. The gas flow openings at the inlet and outlet reservoir are provided with a 'T' section tap each. The first prong of the 'T' section is fixed in the reservoir opening; the second prong is used for nitrogen gas flow whereas the remaining prong serves the measurement of absolute pressure through a microtube. The microchannel is fabricated at the Centre of Excellence in Nanoelectronics (CEN) at IIT Bombay. A silicon wafer (100, p-type) with one side polished is used for microchannel fabrication. The microchannel fabrication process starts with wafer cleaning and surface preparation and photo mask preparation followed by positive photo resist coating, prebaking, UV radiation exposure, post exposure baking, developing, wet etching and finally geometry characterization using profilometer. The surface roughness of approximately 0.1 µm is observed for all the microchannels. The microchannel is sealed with a quartz plate using PDMS (Polydimethylsiloxane) bonding. The geometrical parameters of all microchannels are documented in Tables 2–4.

2.3. Experimental procedure

The validation of the experimental set up is performed by measuring the pressure drop for different mass flow rates through a straight microtube (internal diameter of 800 µm). The experimental *fRe* value is compared against the *fRe* value obtained from the correlation of Verma et al. [8]

$$fRe = \frac{64}{1 + 14.88Kn} \tag{1}$$

where *f* = Darcy friction factor. The above correlation was formulated using experimental data from several researchers and is applicable for laminar flow in a smooth circular tube. The deviation in the experimental *fRe* value was observed to be less than 4% of the value obtained from the correlation; thereby the experimental setup and data reduction procedure is considered to be validated.

Thereafter, experiments for diverging microchannel are carried out. The setup leakage testing is performed using the procedure reported in Demsis et al. [15]. The leakage is ensured to be less than 2% of the mass flow rate employed in the measurements. The uncertainty in mass flow rate consists of the combined uncertainty in the measurement and leakages. The absolute static pressure is measured at the inlet and outlet of the diverging microchannel for different mass flow rates of nitrogen at 300 K. The temperature of the gas at inlet and outlet has been explicitly measured (Table 5). The maximum variation in temperature between the inlet and outlet was noted to be 0.8 K for the slip flow and 1.7 K for the continuum flow. Additional confirmation of the temperature variation is obtained through numerical simulation (results presented later in Section 4.1); which indicates that the flow is nearly isothermal. The flow Reynolds number is between 0.4 and 1280 and the Knudsen number is between 0.0005 and 0.10; thereby covering the continuum and slip regimes. The Mach number is between 0.03 and 0.2 for the slip regime. The ranges of test conditions employed in the measurements are tabulated in Tables 2–4.

2.4. Data reduction

The friction factor *f* is estimated using following equation [32] which takes into account both viscous and acceleration/deceleration effects:

$$\Delta P = \frac{G^2}{2} \left[\frac{fL}{D\rho_m} + 2\left(\frac{1}{\rho_o} - \frac{1}{\rho_i}\right) \right] \tag{2}$$

Here ΔP = pressure drop, Pa; *f* = Darcy friction factor; *L* = length of the tube, m; *D* = hydraulic diameter, m; ρ_m = mean density, ρ_o = density at outlet, ρ_i = density at inlet, kg/m³. Using the ideal gas
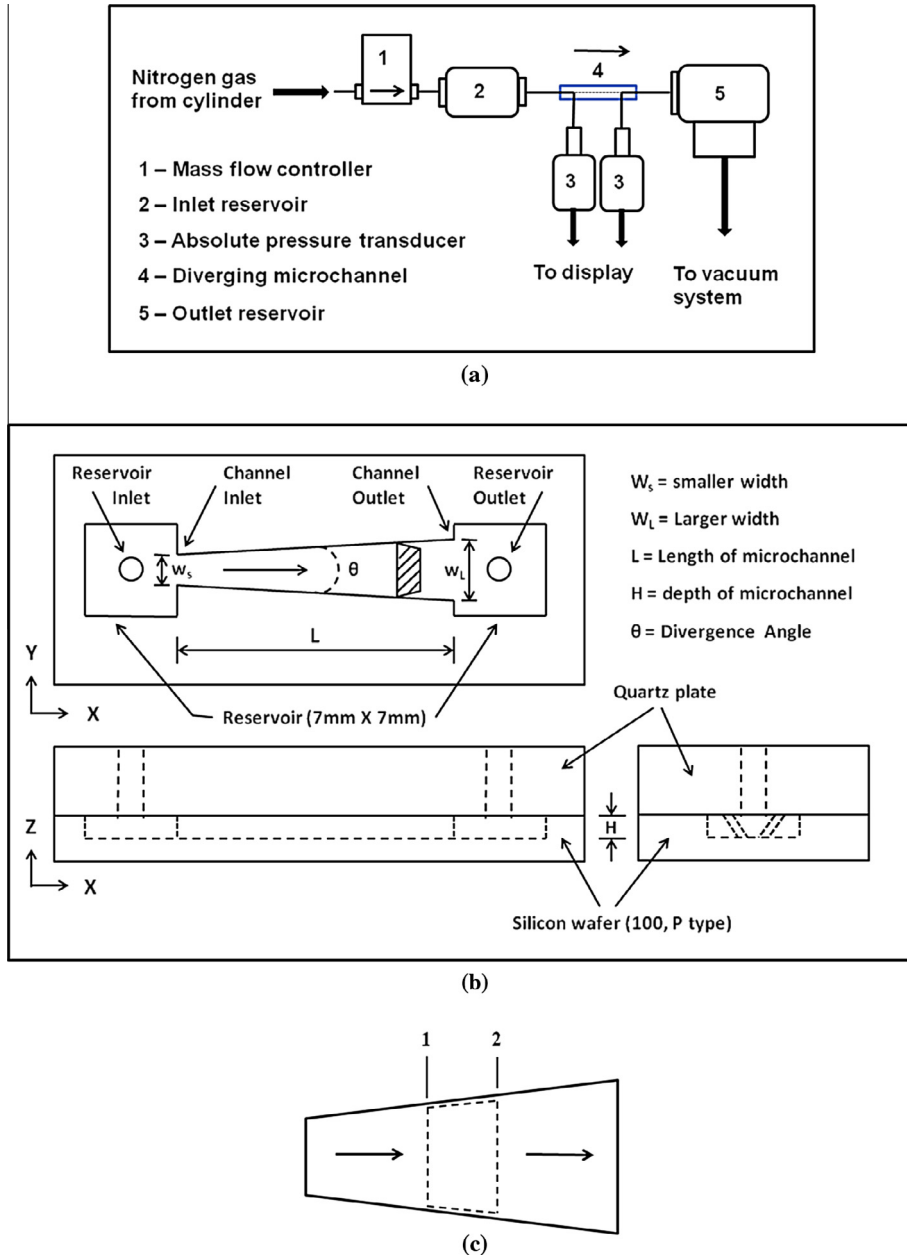
Fig. 1. (a) Schematic diagram of the experimental set up, (b) geometry of gradually diverging microchannel, and (c) control volume for flow through diverging microchannel.

Table 1
Maximum uncertainty in various measured and derived parameters.

Parameter	Maximum uncertainty
Mass flow rate	±2% of full scale
Absolute pressure	±0.15% of the reading
Reynolds number	±2%
Knudsen number	±0.3%
Pressure loss coefficient	±6%
Temperature	±0.7 K

equation and rearranging terms of inlet and outlet pressures we obtain

$$f = (P_i^2 - P_o^2)\left[\frac{1}{G^2 RT} - \frac{1}{P_i P_o}\right]\frac{D}{L} \quad (3)$$

where P_i = pressure at inlet, Pa; P_o = pressure at outlet, Pa; R = specific gas constant, J/kg K; and T = temperature of gas, K. In the above equation G is mass velocity given by

$$G = \frac{\dot{m}}{A} \quad (4)$$

where $\dot{m}$ = mass flow rate, kg/s; A = area of cross section, m². In this work D is considered as the hydraulic diameter at the mid-section of diverging microchannel for obtaining the friction factor. Other definitions of hydraulic diameter are explored later in Section 5.

The Reynolds number and Knudsen number [13] are defined as follows:

$$Re = \frac{\rho U D_h}{\mu} = \frac{G D_h}{\mu} \quad (5)$$

$$Kn = \frac{\lambda}{D_h} = \frac{\mu \sqrt{\frac{\pi RT}{2}}}{p D_h} \quad (6)$$

Here ρ = gas density, kg/m³; U = average velocity, m/s; D_h = hydraulic diameter, m; μ = dynamic viscosity, Pa s; R = specific gas constant, J/kg K; T = temperature of gas, K. The Reynolds number

Table 2
Range of test conditions and geometrical parameters of different divergence angle microchannels with constant hydraulic diameter and length.

Parameter	Micro channel 1	Micro channel 2	Micro channel 3	Micro channel 4	Uncertainty	Unit
Smaller width (w_s)	293	291	291	289	+2	μm
Larger width (w_L)	1680	3077	4480	5902	+2	μm
Length (L)	20	20	20	20	−0.1	mm
Depth (H)	79	78	78	76	±1	μm
Divergence angle (θ)	4	8	12	16	0.5	deg
Hydraulic diameter at mid length	143	147	150	147	+1.33	μm
Mass flow rate	1.87×10^{-8}–3.74×10^{-6} (1–200 sccm)				±2%	kg/s
Inlet pressure	4085–118,934				±0.15%	Pa
Outlet pressure	415–11,148				±0.15%	Pa

Table 3
Range of test conditions and geometrical parameters of different hydraulic diameter microchannels with constant divergence angle and length.

Parameter	Micro channel 1	Micro channel 2	Micro channel 3	Uncertainty	Unit
Smaller width (w_s)	267	291	276	+2	μm
Larger width (w_L)	3064	3077	3073	+2	μm
Length (L)	20	20	20	−0.1	mm
Depth (H)	62	78	95	±1	μm
Divergence angle (θ)	8	8	8	0.5	deg
Hydraulic diameter at mid length	118	147	177	+1.33	μm
Mass flow rate	1.87×10^{-8}–3.74×10^{-6} (1–200 sccm)			±2%	kg/s
Inlet pressure	3740–113,630			±0.15%	Pa
Outlet pressure	425–10,777			±0.15%	Pa

Table 4
Range of test conditions and geometrical parameters of different length microchannels with constant divergence angle and hydraulic diameter.

Parameter	Micro channel 1	Micro channel 2	Micro channel 3	Uncertainty	Unit
Smaller width (w_s)	310	312	309	+2	μm
Larger width (w_L)	1710	3113	4508	+2	μm
Length (L)	10	20	30	−0.1	mm
Depth (H)	84	83	83	±1	μm
Divergence angle (θ)	8	8	8	0.5	deg
Hydraulic diameter at mid length	152	156	159	+1.33	μm
Mass flow rate	1.87×10^{-8}–3.74×10^{-6} (1–200 sccm)			±2%	kg/s
Inlet pressure	4693–106,938			±0.15%	Pa
Outlet pressure	466–10,571			±0.15%	Pa

Table 5
Gas temperature measurements.

Microchannel (divergence angle)	Knudsen number at outlet	Gas temperature in Kelvin	
		Inlet	Outlet
4 deg.	0.10	300	299.3
	0.004	300.1	298.6
8 deg.	0.09	300.2	299.5
	0.004	300	298.3
12 deg.	0.10	300.1	299.3
	0.004	300	298.4
16 deg.	0.10	300.1	299.3
	0.005	299.9	298.2

is also calculated (Eq. (5)) corresponding to mid-section of the microchannel. The effect of divergence angle, hydraulic diameter and length on the non-dimensional friction constant (Poiseuille number) is presented next.

3. Experimental results

The experiments are performed for different divergence angles (4°, 8°, 12° and 16° with hydraulic diameter 147 μm and length 20 mm), hydraulic diameters (118, 147 and 177 μm with 8° diver-

gence angle and length 20 mm) and lengths (10, 20 and 30 mm with 8° divergence angle and hydraulic diameter 156 μm) of diverging microchannels. That is, the measurements were done for a total of nine different configurations for a Knudsen number range of 0.0005–0.10. The effect of diverging angle, hydraulic diameter and length of microchannel on pressure drop and Poiseuille number is investigated in this section.

3.1. Measurement of static pressure drop

The static pressure at the reservoir inlet and outlet of the diverging microchannel (refer Fig. 1b) is measured for different mass flow rates (1.87×10^{-8} to 3.74×10^{-6} kg/s). The pressure ratio range between the reservoir inlet and outlet is 7–12. The effect of divergence angle, hydraulic diameter and length of microchannel on pressure drop is presented in this section.

The pressure drop is measured for diverging microchannels of 4°, 8°, 12° and 16° divergence angle with the same hydraulic diameter, microchannel depth and length. Fig. 2a indicates that the pressure drop varies nonlinearly with the mass flow rate similar to gas flow through a straight microchannel. This non-linearity is however not so apparent here because of the log scale employed for plotting. In contrast, a linear variation in pressure drop was reported by Duryodhan et al. [19] in case of incompressible liquid flow through the same microchannel. The pressure drop decreases as the divergence angle increases from 4° to 12° for a given mass

flow rate. The pressure drop for 16° microchannel is marginally larger (maximum deviation of 7%) than that of 12° microchannel.

The pressure drop due to viscous component (the first term in Eq. (2)) is plotted in Fig. 2b. The viscous pressure drop increases with an increase in the diverging angle. The viscous pressure drop increases nonlinearly and approaches the total pressure drop with increasing rarefaction. It indicates that the acceleration effect due to compressibility (pressure gradient) is negated by the diverging microchannel geometry. It is concluded that the viscous component dominates over the acceleration component in case of rarefied gas flow through diverging microchannel; this appears surprising because the pressure ratio across the microchannel is more than 11. The diverging cross sectional area restricts the acceleration even when there is a higher pressure ratio.

Another set of measurements were performed to study the effect of hydraulic diameter on the pressure drop. For this, diverging microchannels of 118, 147 and 177 μm hydraulic diameter with same divergence angle (8°), depth and length were employed. Fig. 3a again shows a nonlinear pressure drop variation with the mass flow rate; note that the results have been plotted on log scale. That is, pressure drop is an inverse function of the mean hydraulic diameter of the diverging microchannel (as expected); which is similar to a straight microchannel.

The pressure drop is further measured for diverging microchannels of three different lengths (10, 20 and 30 mm), with the same hydraulic diameter (155 μm), divergence angle (8°) and depth. Fig. 3b shows the effect of mass flow rate and length on the pressure drop. It is indicated that the pressure drop becomes a weak function of microchannel length (for the parameter range investigated) with an increase in microchannel length or an increase in pressure drop.
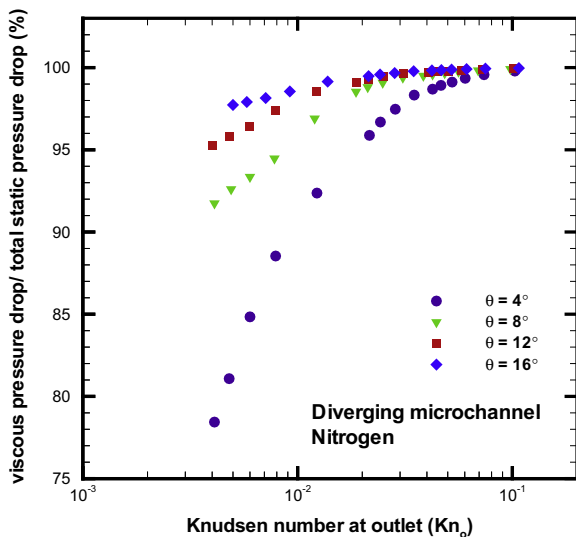
3.2. Friction constant (fRe)

Fig. 4 shows the variation in fRe with rarefaction for 4°, 8°, 12° and 16° diverging microchannels. The fRe value is independent of Kn for larger Knudsen numbers ($Kn_o > 0.02$); however the friction constant increases with an increase in the divergence angle. The
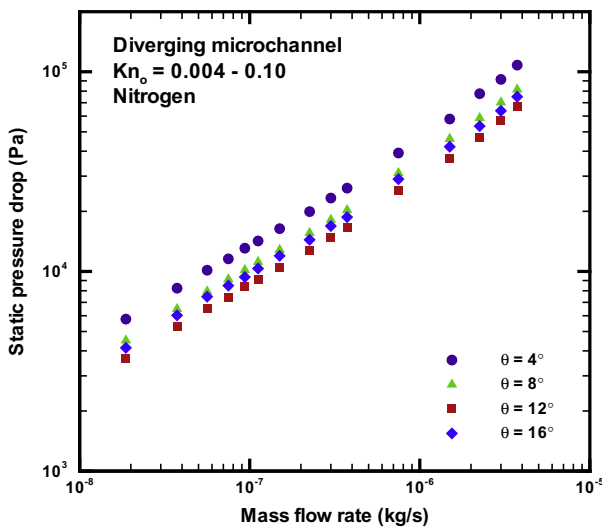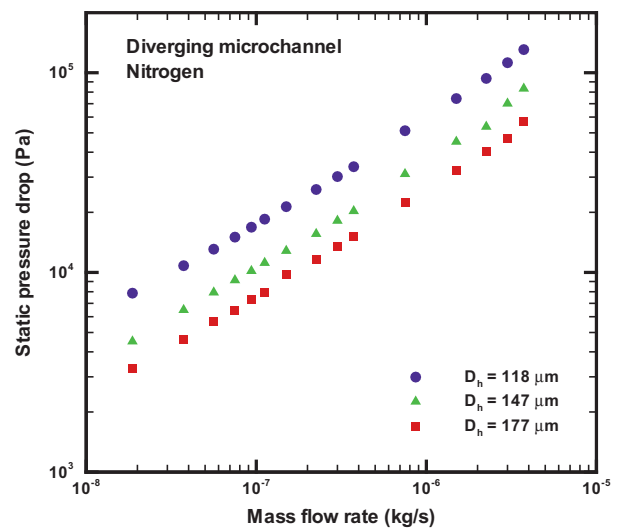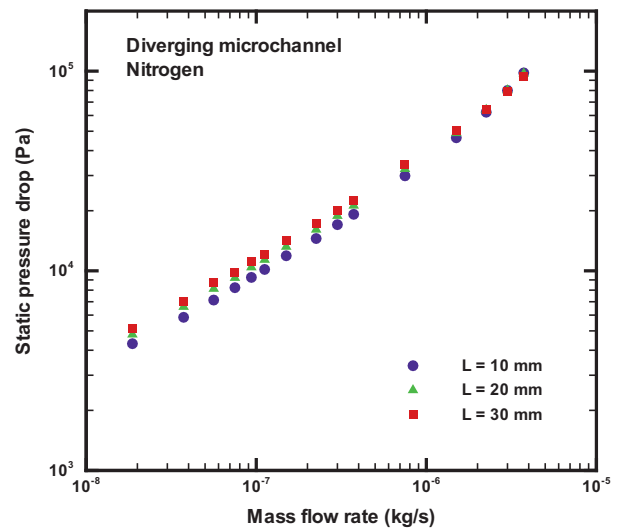

Fig. 2. Effect of diverging angle on experimental (a) static pressure drop and (b) viscous pressure drop (mean hydraulic diameter $D_h = 147$ μm, length $L = 20$ mm, θ = full divergence angle).

Fig. 3. Effect of (a) hydraulic diameter on experimental static pressure drop (D_h = mean hydraulic diameter, microchannel length $L = 20$ mm, full divergence angle $\theta = 8°$) and (b) length on static pressure drop ($D_h = 155$ μm, $\theta = 8°$).
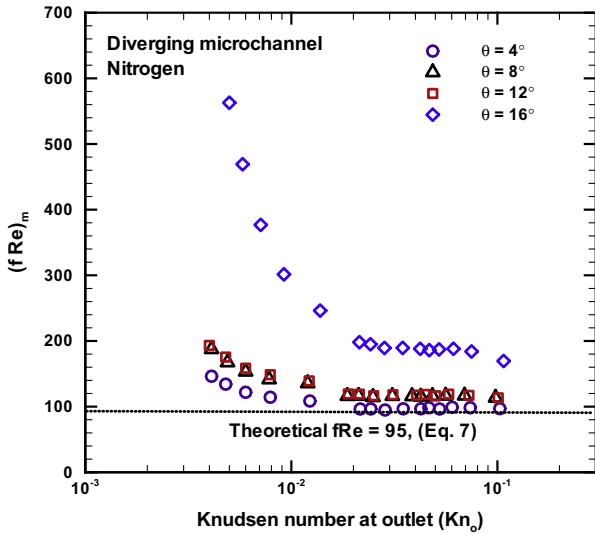
Fig. 4. Effect of diverging angle on experimental $(fRe)_m$ [$(fRe)_m = fRe$ on the basis of mid section of the microchannel, mean hydraulic diameter $D_h = 147$ μm, microchannel length $L = 20$ mm].

negligible acceleration effect is indicated for larger Kn values from Fig. 2b; absence of acceleration effect can be noted by a constant value of fRe in Fig. 4. This shows that the non-dimensionalization of the pressure drop into friction factor does not nullify the effect of acceleration (which is a function of the mass flow rate).

The variation in fRe with rarefaction for 118, 147 and 177 μm hydraulic diameter microchannels is shown in Fig 5a. The fRe increases with decrease in hydraulic diameter; however it is independent of Kn for larger Knudsen numbers ($Kn_o > 0.02$). The fRe variation with rarefaction for 10, 20 and 30 mm microchannel length is plotted in Fig. 5b. The Poiseuille number decreases with decreasing length.

The fRe value is also compared against that for a straight microchannel based on the inlet geometry with incompressible flow. The fRe value is estimated using correlation proposed by Morini [3] for uniform microchannel (Eq. (7)) using aspect ratio at the inlet section of the microchannel.

$$f_f Re = 24 - 42.267\gamma + 64.272\gamma^2 - 118.42\gamma^3 + 242.12\gamma^4$$
$$- 178.79\gamma^5 \quad (0 < \gamma < 0.707) \tag{7}$$

Here f_f = Fanning friction factor, Re = Reynolds number, γ = aspect ratio (ratio of microchannel depth to width (average of top and bottom width) at a specified location). The theoretical fRe value ($fRe = 95$, here $f = 4f_f$) is represented by a single line in Fig. 4 due to approximately uniform aspect ratio (maximum deviation 3%) of inlet section for all the cases. The experimental fRe value ($fRe \approx 100$) for 4°, 8° and 12° channels is in agreement with the theoretical fRe value (Fig. 4).

The fRe for nitrogen gas flow in the near continuum regime ($Kn_m = 0.004$–0.015) is compared with the water flow through diverging microchannel [19]. This comparison is shown in Fig. 6 for flow through 4°, 8° and 12° diverging microchannel. The 16° microchannel is not considered due to flow separation in case of water flow. A maximum deviation of 10% is observed in the fRe variation of water flow with reference to nitrogen flow. This deviation can be attributed to the measurement uncertainty (mass flow metering device and pressure gauges are different for the two fluids) and the fact that Knudsen number for water flow is of lower value than that of the nitrogen flow. The comparison serves to enhance confidence in the presented results.
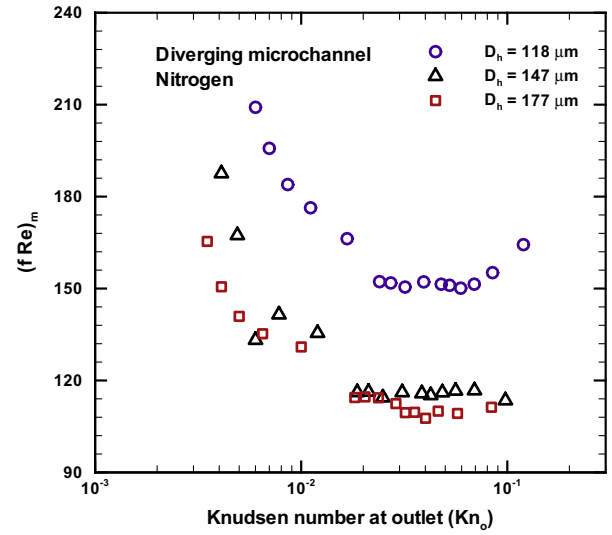
(a)
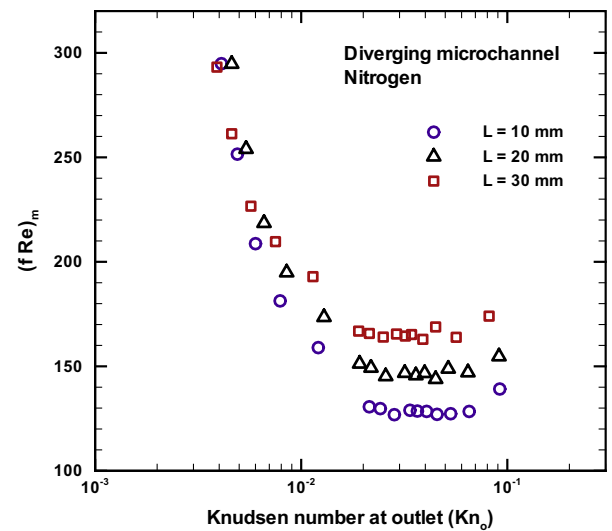
(b)

Fig. 5. Effect of (a) hydraulic diameter on experimental $(fRe)_m$ [$(fRe)_m = fRe$ on the basis of mid section of the microchannel, D_h = mean hydraulic diameter, microchannel length $L = 20$ mm, full divergence angle $\theta = 8°$) and (b) length on experimental $(fRe)_m$ [$(fRe)_m = fRe$ on the basis of mid section of the microchannel $D_h = 155$ μm, $\theta = 8°$].

4. Numerical methodology

The experimental analysis presented in the previous section explores the flow behavior on the basis of the overall pressure drop measurement for different mass flow rates. The numerical methodology is employed for obtaining local variation in flow parameters, as discussed in this section. The numerical results are validated on the basis of experimental measurements.

4.1. Navier–Stokes based simulations

A commercial CFD solver (Fluent [33], Version 6.3.26) is used for obtaining the numerical results. We apply first-order Maxwell's slip boundary condition (Eq. (8)) while solving the Navier–Stokes equations.
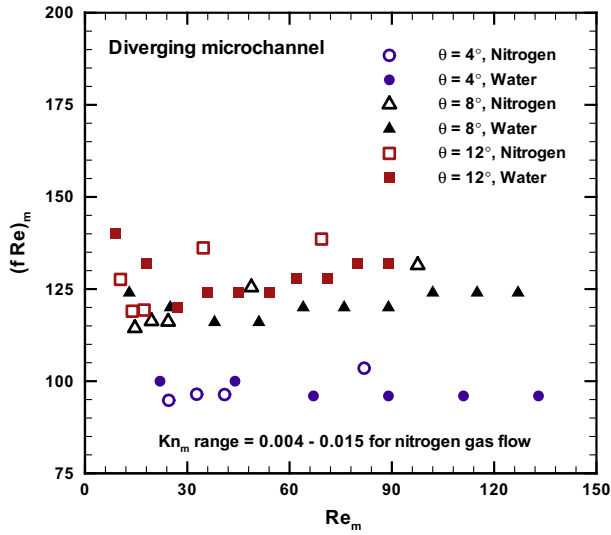
Fig. 6. Comparison of Poiseuille number (*fRe* – experimental) between nitrogen gas flow and water flow [19] through diverging microchannel [θ = full divergence angle, mean hydraulic diameter D_h = 147 µm, length L = 20 mm, $(fRe)_m = fRe$ on the basis of mid section of the microchannel].

Table 6
Grid independence test.

Number of cells	Static pressure drop (Pa)	% deviation with reference to finest mesh
1,00,000 (40 × 10 × 250)	37,519	1.11
2,00,000 (40 × 10 × 500)	37,548	1.04
4,00,000 (40 × 10 × 1000)	37,591	0.93
8,00,000 (40 × 20 × 1000)	37,942	–

$$u_g - u_w = -C_1 \cdot \lambda \cdot \left(\frac{\partial u}{\partial y}\right)_{wall} \tag{8}$$

$$C_1 = \frac{2 - \sigma}{\sigma} \tag{9}$$

Here u_g = gas velocity (m/s), u_w = velocity of wall (m/s), C_1 = slip coefficient, λ = mean free path of molecules (m), $\partial u/\partial y$ = velocity gradient, σ = tangential momentum accommodation coefficient. Earlier studies [5,13,34–36] suggest that the solution of Navier–Stokes equation using first order slip boundary condition can predict the solution in the early part of the slip flow regime. Hence, first order slip boundary condition has been applied in the current work. The governing equations are discretized using the finite volume methodology. The ideal gas law is applied for density variation. The "Low-Pressure Boundary Slip" module is invoked for the slip boundary condition with "Pressure Based" solver and SIMPLE algorithm for pressure–velocity coupling. The value of tangential momentum accommodation coefficient (TMAC) is employed on the basis of investigation reported by Agrawal and Prabhu [37]. A value of 0.926 is recommended by them (on the basis of experimental data of several researchers) for commonly employed surfaces and most gases over a large *Kn* range; therefore, TMAC value of 0.926 is employed in this work. The other boundary conditions are mass flow rate (at inlet) and pressure boundary condition (at outlet).

The three-dimensional computational domain of diverging microchannel (Fig. 1b) is discretized with quadrilateral face elements and hexahedral volume elements. A grid independence test is conducted and the results are tabulated in Table 6. Grid size of 100,000 hexahedral elements is employed in all simulations on the basis of this test. The residue of 10^{-11} is set as convergence criteria due to relatively small mass flow rate involved.
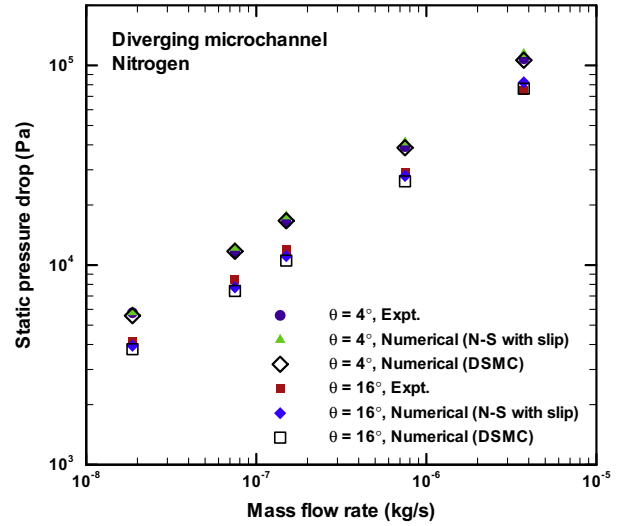
(a)
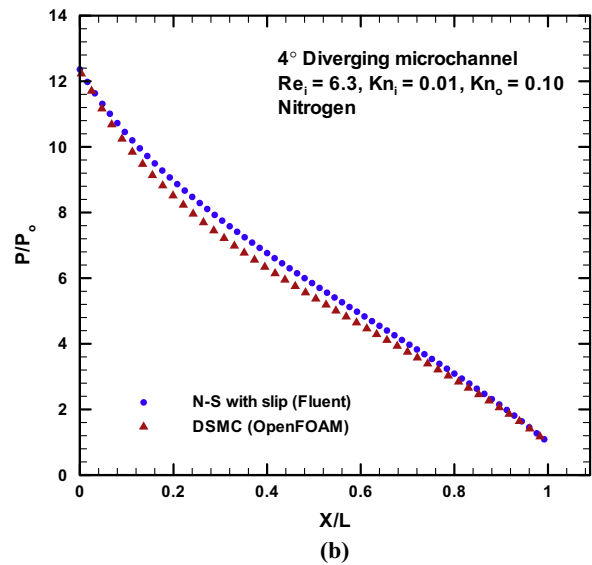
(b)

Fig. 7. Comparison of (a) experimental static pressure drop with N–S and DSMC simulations based pressure drop and (b) static pressure variation between Navier–Stokes solution and DSMC method (mean hydraulic diameter D_h = 147 µm, length L = 20 mm).

The numerical simulation based overall pressure drop is compared with the experimental value and DSMC results (explained in the next section) for various mass flow rates. The comparison is performed over a wide range of flow rates (Fig. 7a; note log scale) and two different divergence angle microchannels. A maximum deviation of 10% and 7% is observed in the pressure drop with respect to the experimental values and the DSMC results respectively. The deviation can be attributed to the combined uncertainty in (i) characterization of the microchannel dimensions (Table 2), (ii) experimental measurements (Table 1) and (iii) numerical solution (Table 6). The comparison serves to validate the numerical results.

4.2. Direct Simulation Monte Carlo based calculation

The numerical solution of Navier–Stokes equations with slip boundary condition is compared with direct simulation Monte Carlo (DSMC) results for 4° diverging microchannel in Fig. 7b. The

DSMC code has been executed under the framework of OpenFOAM [38]. OpenFOAM is an open-source C++ computational fluid dynamics toolbox. The computational domain is meshed using structured uniform grids with about 90,000 cells and 1,000,000 DSMC simulator particles are used to conduct the simulations. In the present study, the Variable Hard Sphere (VHS) collision model and Larsen-Borgnakke internal energy redistribution model [39] have been used to perform inter-molecular collisions. A comprehensive study about DSMC solver is reported elsewhere [40–42]. The solution procedure is done in parallel on four processors. The nitrogen gas flow is simulated according to experimental data in which the surface and inlet gas temperature are set to 300 K. The outlet pressure is set to 435 Pa and the inlet to outlet pressure ratio is about 12.35. The Knudsen numbers at the inlet and outlet are 0.01 and 0.1, respectively. The equality of the mass flow rate at inlet and outlet is considered as the convergence criteria. A maximum deviation of 7% is observed in pressure variation obtained from the Navier–Stokes solution and measured pressure drop with reference to the DSMC results. This comparison validates the numerical results obtained from Navier–Stokes equations with first order slip boundary condition in the slip regime.

5. Numerical results

The local behavior of rarefied gas flow through diverging microchannel is analyzed in this section. The numerical solution of Navier–Stokes equations with first order slip boundary condition is obtained for four diverging microchannels. The static pressure and temperature variation, velocity distribution, wall shear stress and force balance is presented in this section.

5.1. Static pressure and temperature variation

The non-dimensional static pressure variation along the microchannel axis is plotted in Fig. 8a for four divergence angles (4°, 8°, 12°, 16°) with outlet Knudsen number of 0.1. The figure indicates that nonlinearity in static pressure variation increases with an increase in the divergence angle. The nonlinearity is indicated for $X/L < 0.4$ while linear pressure variation is evident for $0.4 < X/L < 0.8$ from Fig. 8a (where X is the axial distance from the microchannel inlet and L is the length of the microchannel). The figure indicates that the effect of divergence is limited to $X/L < 0.4$, as analyzed further in Section 6. Notice that the overall pressure drop decreases as the divergence angle increases from 4° to 12°; whereas it is marginally larger for 16° microchannel as compared to 12° microchannel, in agreement with the experimental result (Fig. 2a).

The temperature variation along the flow direction for $Kn_o = 0.10$ is plotted in Fig. 8b, for 4° and 16° microchannels. The figure indicates that the maximum variation in temperature is 0.5 K even when the pressure ratio across the microchannel is more than 11; which is comparable with the temperature measurements for the same case shown in Table 5. This reinforces that gas flow through a diverging microchannel is nearly isothermal, at least for the parameter range investigated herein.

5.2. Velocity distribution and wall shear stress

The axial velocity (non-dimensionalized with sonic speed and the lateral distance with the microchannel depth) variation along the microchannel axis is plotted in Fig. 9 for four divergence angles (4°, 8°, 12°, 16°), with the outlet Knudsen number of 0.1. A nonlinear central velocity variation is noted from the figure. Notice deceleration of the flow for $X/L < 0.4$. The central velocity remains approximately constant for $0.4 < X/L < 0.8$; while the flow acceler-

ates for $X/L > 0.8$. In contrast, Duryodhan et al. [19] noted a constant central velocity for $X/L > 0.4$ with incompressible flow. Notice from the figure that the rate of deceleration increases with an increase in the divergence angle; whereas the rate of acceleration is higher in the smaller divergence angle microchannel. The larger deceleration indicates more pressure recovery whereas larger acceleration indicates more pressure loss. Therefore static pressure drop decreases with an increase in the divergence angle. The effect of divergence angle on deceleration and acceleration of rarefied gas flow is discussed further in Section 6.

The axial velocity distribution along the central planes of the microchannel is shown in Fig. 10a for 4° and in Fig. 11a for 16° angle microchannels. The depth of the microchannel is constant whereas the width varies, because of which the y/H values for different profiles are different. Note that $y = 0$ corresponds to the centerline. The velocity profile is relatively flat for $X/L > 0.20$ in case of
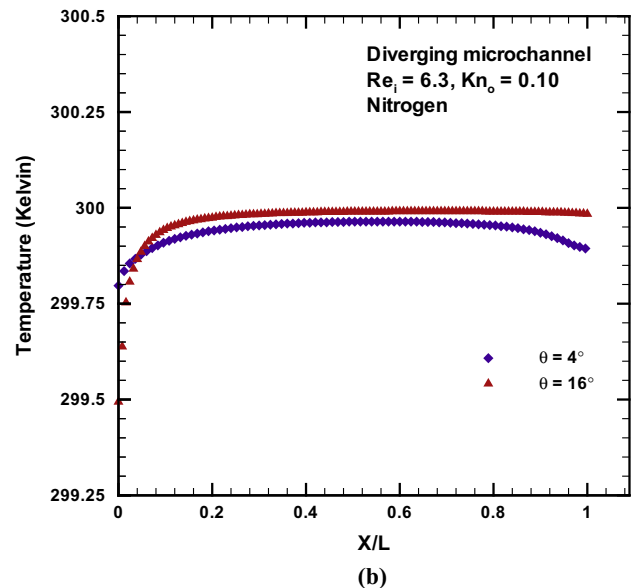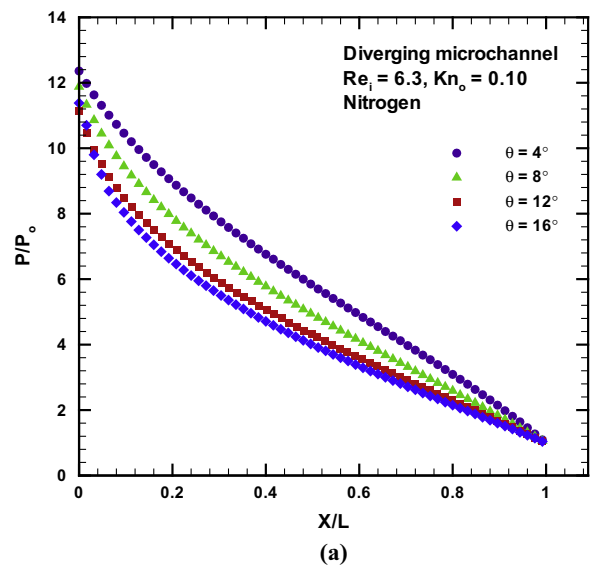

(a)

(b)

Fig. 8. Effect of diverging angle on (a) static pressure variation (N–S solution) and (b) temperature variation (N–S solution) along the channel axis (mean hydraulic diameter $D_h = 147$ μm, microchannel length $L = 20$ mm, θ = full divergence angle, Re_i = Reynolds number at channel inlet, Kn_o = Knudsen number at channel outlet, P = local static pressure, P_o = static pressure at channel outlet, X = axial distance from channel inlet).
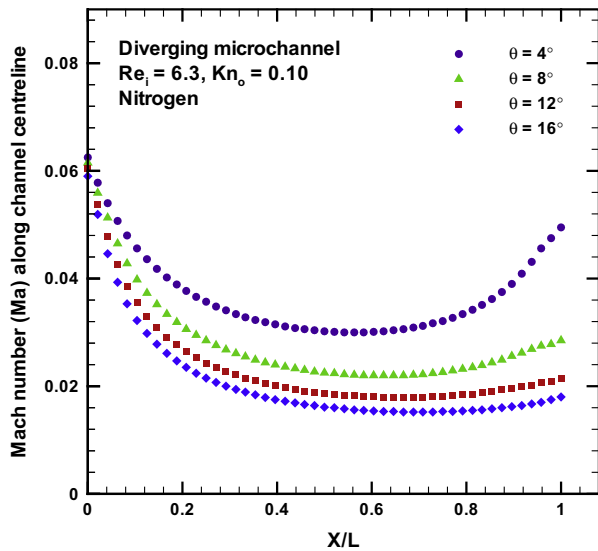
Fig. 9. Effect of diverging angle on centerline velocity (N–S solution) variation (mean hydraulic diameter D_h = 147 μm, length L = 20 mm, θ = full diverging angle, Re_i = Reynolds number at channel inlet, Kn_o = Knudsen number at channel outlet, X = axial distance from channel inlet).

4° microchannel, whereas in case of 16° microchannel it appears relatively flat for X/L > 0.05. This shows a transition in flow behavior from micro-duct to microchannel due to an increase in the local aspect ratio [4] at these locations. The flow deceleration stops approximately at X/L = 0.4, further downstream up to X/L = 0.8 flow resumes a uniform velocity for both the cases. It can be correlated to the nonlinearity in local pressure variation for X/L < 0.4 and a linear pressure variation further downstream up to X/L = 0.8 as noted in Section 5.1.

The axial velocity distribution along the central XZ plane of the diverging microchannel is shown in Fig. 10b for 4° and in Fig. 11b for 16° angle cases (z = 0 corresponds to the bottom wall of the microchannel). The velocity profile is similar to parabolic velocity profile at the channel inlet and further downstream the central velocity is uniform for 0.4 < X/L < 0.8. The velocity contour along central XY, XZ and YZ plane are shown in Fig. 10c and d for 4° microchannel (Fig. 11c and d for 16° microchannel).

The absence of flow reversal can be noted from Fig. 11 in case of 16° microchannel. In contrast, White [43] reported flow reversal for incompressible flow through 15° micro-diffuser and Duryodhan et al. [19] noted flow reversal for incompressible flow through 16° diverging microchannel. The acceleration of the flow due to reduction in density or pressure, which partly counters the deceleration due to increase in cross-sectional area, causes this delay in flow separation. The slip velocity is shown in Fig. 12a for 4° and 16° angle cases. The maximum slip velocity is noted at the microchannel inlet due to maximum velocity gradient at the wall of the microchannel inlet section. The slip velocity follows the centerline velocity distribution qualitatively. Fig. 12a indicates larger slip velocity in 4° microchannel than 16° microchannel owing to larger velocity as compared to 16° microchannel.

The wall shear stress along the central plane of side and top/bottom wall of the microchannel is shown in Fig. 12b for 4° and 16° diverging angle. The top/bottom wall shear stress for 4° microchannel decreases nonlinearly for X/L < 0.4, becomes constant for 0.4 < X/L < 0.8, and increases nonlinearly further downstream. In case of 16° microchannel, top/bottom wall shear stress decreases from the inlet to the outlet of the microchannel. The side wall shear stress for 4° and 16° channels drops with nonlinear variation up to X/L = 0.2 and becomes constant further downstream. Fig. 12b indi-

cates a larger wall shear stress for 4° microchannel due larger velocity as compared to 16° microchannel.

5.3. Force balance

As noted earlier in Section 3.1, the pressure drop between inlet and outlet of the microchannel is dominated by viscous effect. In order to understand this behavior, it is important to understand the variation of forces acting on a fluid element in the microchannel, and the relative contribution of the various forces. A force balance for a finite size control volume (see Fig. 1c) is therefore undertaken. From (Pressure force = Inertia force + Shear force) we obtain:

$$d(pA) = \rho u^2 dA + \tau_w dA_s \tag{10}$$

where ρ = density, kg/m³; u = axial velocity, m/s; p = static pressure, Pa; A = cross sectional area (m²); τ_w = shear stress at the wall (N/m²) and A_s = surface area (m²). The force balance for 12° diverging microchannel is plotted in Fig. 13. The gas flow enters the diverging microchannel from the inlet reservoir through a relatively small trapezoidal cross section (area ratio ≈ 30). The sudden contraction causes substantial flow acceleration from just upstream of the microchannel inlet (not shown); thereby flow reaches maximum velocity at the microchannel inlet. Therefore, both inertia and viscous forces are maximum at the microchannel inlet (Fig. 13); leading to large pressure force. The pressure force, inertia force and shear force decreases non-linearly up to X/L = 0.4; further downstream, the inertial force becomes approximately zero, and the pressure force is balanced by the viscous force. The figure indicates that the magnitude of viscous force is larger than the inertia force throughout the microchannel; which is in line with the observation noted earlier from the pressure drop measurement (Fig. 2b). Therefore, it is concluded that the viscous force has a greater contribution than the inertia force in the overall pressure drop for low Mach number rarefied gas flow through diverging microchannel.

6. Discussion

The concept of equivalent hydraulic diameter is presented in this section. The effect of divergence on static pressure, velocity, wall shear stress and force balance is also discussed. The absence of flow reversal in 16° channel is further analyzed, and correlation for non-dimensional pressure drop for diverging microchannel is proposed.

6.1. Equivalent hydraulic diameter

The definition of characteristic dimension in the case of varying cross-section micro channel is somewhat ambiguous. The hydraulic diameter can be considered at the inlet, middle or outlet as the characteristic length. Generally the hydraulic diameter is calculated on the basis of the midpoint location for the purpose of non-dimensionalization. However, these estimations do not represent the correct characteristic scale for diverging microchannels [19]. The mean integral value of hydraulic diameter calculated along the profile is somewhat a better estimate.

Here we introduce the concept of equivalent hydraulic diameter, similar to that given by Duryodhan et al. [19]. The equivalent hydraulic diameter is defined as the hydraulic diameter of a non-uniform cross section having the same Poiseuille number (fRe) as that of a uniform cross section (see Fig. 14a). The equivalent hydraulic diameter facilitates calculation of parameters like fRe for the diverging microchannel using the conventional correlation of uniform microchannel. The algorithm for obtaining the location of equivalent hydraulic diameter is illustrated in Fig. 14b. The
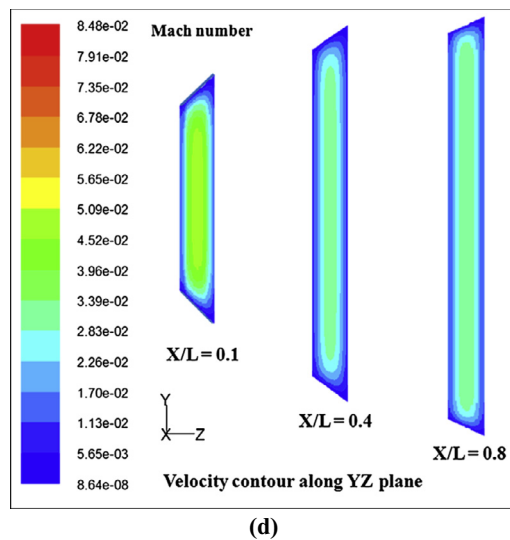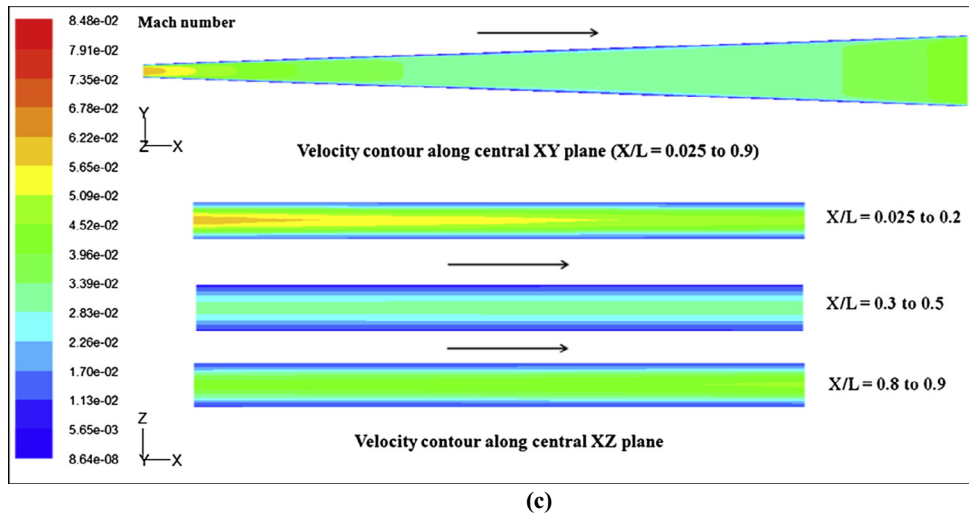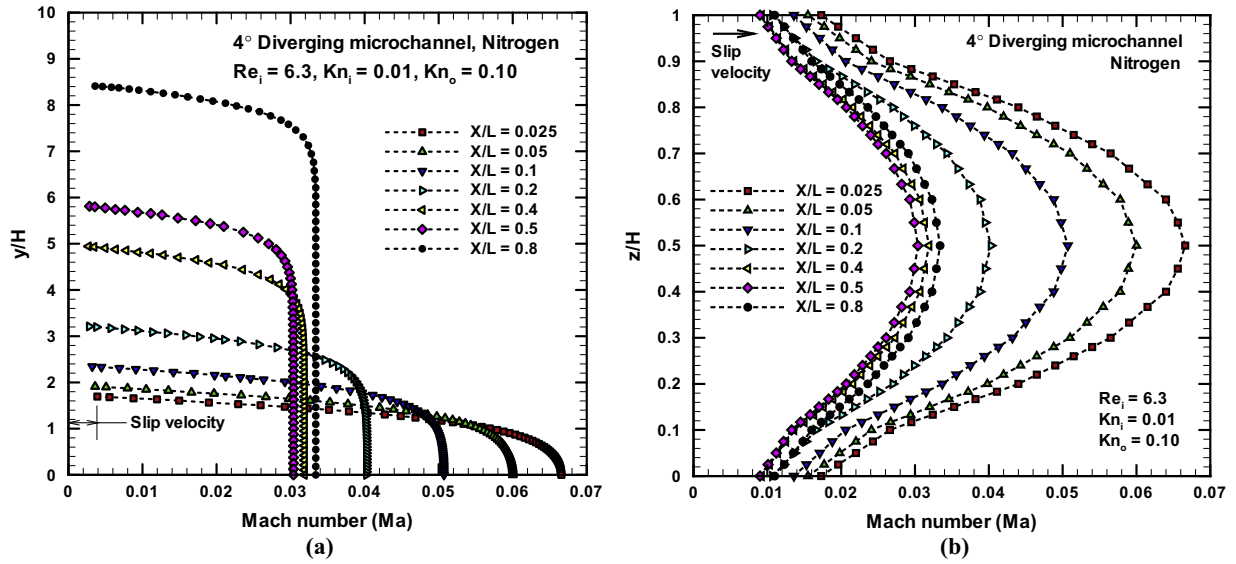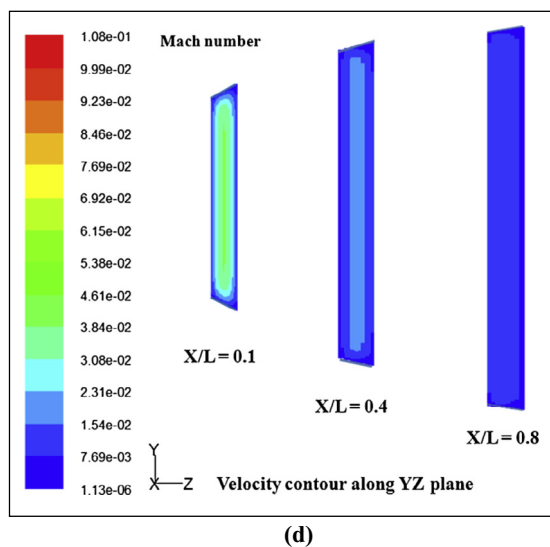
(a)

(b)

(c)

(d)

Fig. 10. Velocity distribution (N–S solution) in 4° diverging microchannel along (a) central XY plane, (b) central XZ plane and velocity contour along, (c) central XY, XZ plane, and (d) YZ plane (mean hydraulic diameter D_h = 147 μm, length L = 20 mm, Re_i = Reynolds number at channel inlet, Kn_i and Kn_o = Knudsen number at channel inlet and outlet, X = axial distance from channel inlet, y = distance from central axis in y direction, z = distance from bottom wall of the microchannel in z direction, H = microchannel depth).
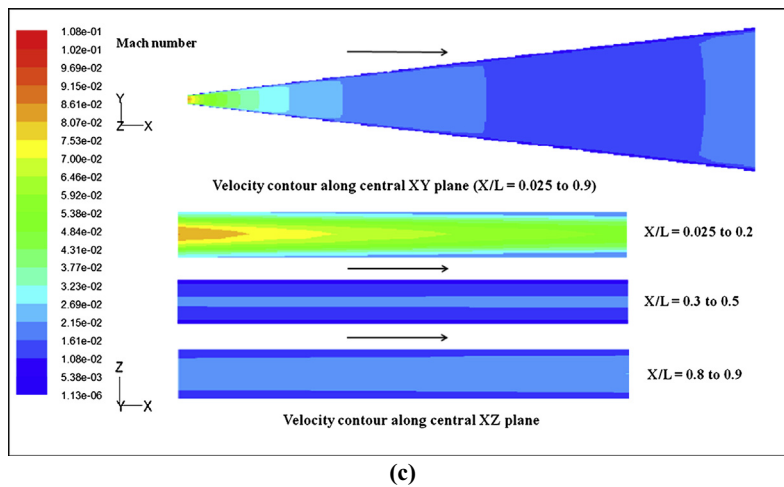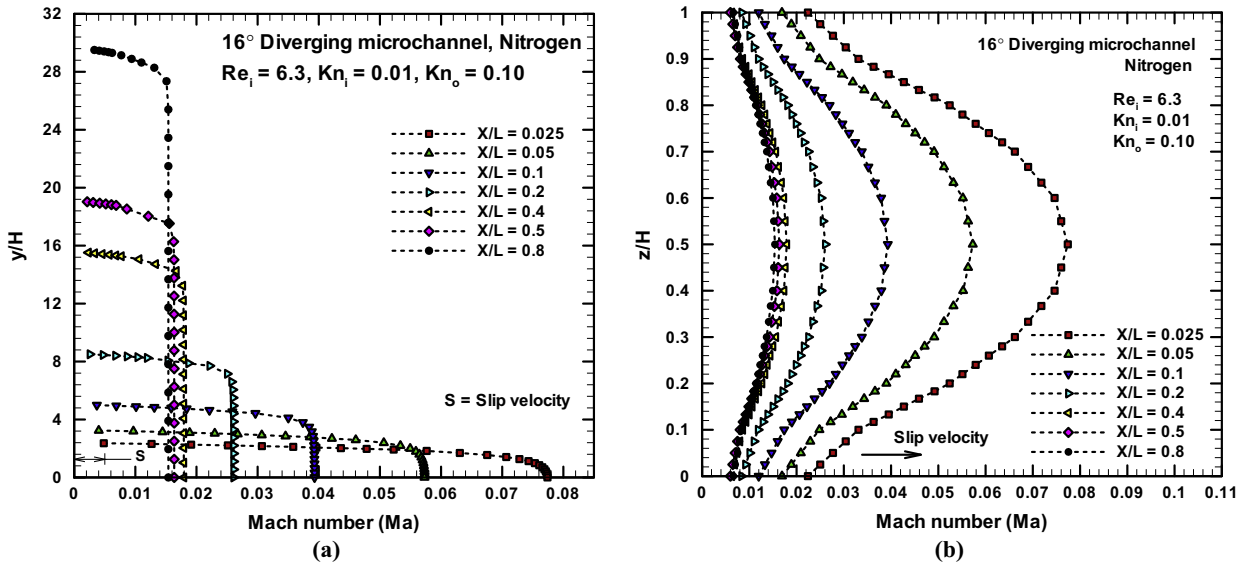
Fig. 11. Velocity distribution (N–S solution) in 16°diverging microchannel along (a) central XY plane, (b) central XZ plane and velocity contour along, (c) central XY, XZ plane, and (d) YZ plane (mean hydraulic diameter D_h = 147 µm, length L = 20 mm, Re_i = Reynolds number at channel inlet, Kn_i and Kn_o = Knudsen number at channel inlet and outlet, X = axial distance from channel inlet, y = distance from central axis in y direction, z = distance from bottom wall of the microchannel in z direction, H = microchannel depth).
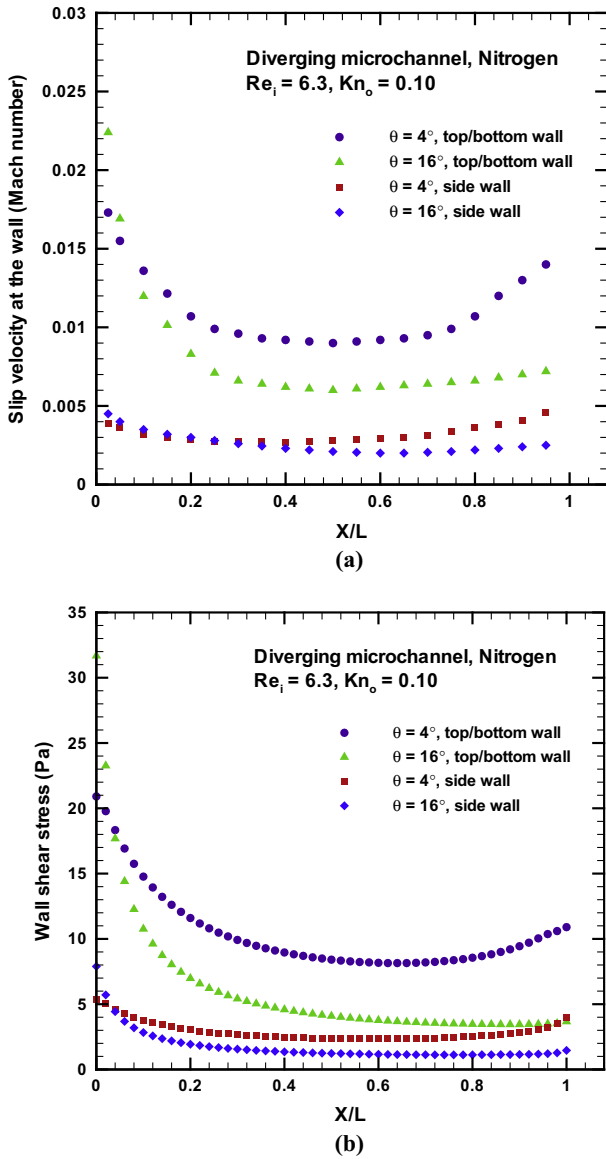
(a)

(b)

Fig. 12. Effect of diverging angle on (a) slip velocity (N–S solution) at the wall and (b) wall shear (N–S solution) stress (mean hydraulic diameter D_h = 147 μm, length L = 20 mm, θ = full diverging angle, Re_i = Reynolds number at channel inlet, Kn_o = Knudsen number at channel outlet, X = axial distance from channel inlet.)

equivalent hydraulic diameter can be noted as we obtain the location from the algorithm.

The algorithm from Fig. 14b is applied for the entire experimental dataset. The location of equivalent hydraulic diameter for the present work (Kn_o = 0.004–0.10) lies between $L/3$ and $L/12.5$ (where L is the microchannel length), from the inlet of diverging microchannel. (For comparison, the equivalent hydraulic diameter lies at $L/3$ in the continuum case [19]). This result indicates that although the location of the equivalent hydraulic diameter is independent of the divergence angle, microchannel length, and mass flow rate (reinforcing the observation of Duryodhan et al. [19]); it depends on the amount of rarefaction. The equivalent hydraulic diameter approaches the inlet of the diverging microchannel as the Knudsen number increases. Thus, the hydraulic diameter at the smaller section can be considered as the characteristic length for highly rarefied ($Kn_o > 0.10$) gas flow through diverging microchannels.

The concept of equivalent hydraulic diameter has been further confirmed through numerical simulations. Four diverging angle
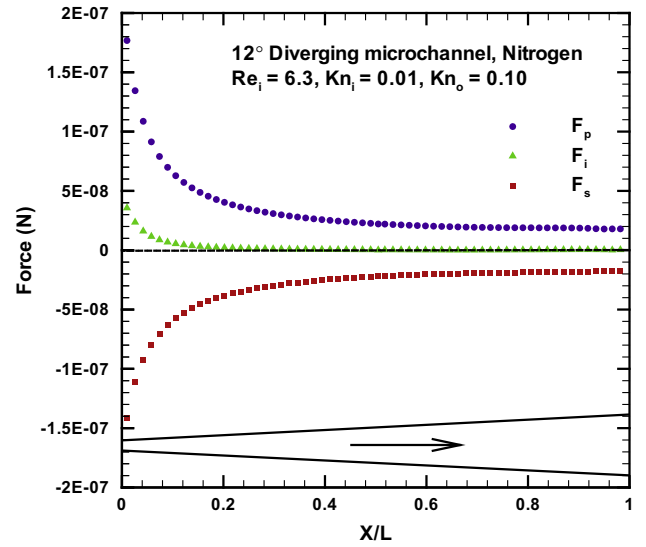

Fig. 13. Force balance (N–S solution) for diverging microchannel (mean hydraulic diameter D_h = 147 μm, length L = 20 mm, θ = full diverging angle, Re_i = Reynolds number at channel inlet, Kn_o = Knudsen number at channel outlet, X = axial distance from channel inlet, Fp = pressure force, Fi = inertia force, Fs = shear force).

(4°, 8°, 12° and 16°) microchannels are designed in such a way that the equivalent hydraulic diameter (at 1/12.5 of microchannel length from inlet section) is the same (D_h = 140 μm) for all the microchannels. The numerical solution obtained for these cases is compared with uniform cross section microchannel of the same hydraulic diameter (D_h = 140 μm) and flow condition as that of the diverging microchannels. The same pressure drop (maximum 7% deviation with reference to uniform cross section microchannel) is obtained for all the cases (Table 7), owing to constant hydraulic diameter. These results suggest that the conventional correlation for uniform microchannel can be applicable to diverging microchannel using equivalent hydraulic diameter concept. This result should be helpful in designing micro-diffusers and micro-pumps. The dependence of the location on the Knudsen number however makes this result less attractive than the continuum case (where it was independent of all governing parameters).

6.2. Effect of divergence on flow behavior

The effect of divergence on rarefaction is shown in Fig. 15a. In the case of a straight tube rarefaction is a function of pressure variation along the length (or mean free path of molecules) due to uniform cross section. However in the case of varying cross section microchannel rarefaction is a function of the hydraulic diameter variation and the pressure variation along the length. Fig. 15a indicates that Knudsen number increases with an increase in diverging angle and increase in hydraulic diameter. The Knudsen number is an inverse function of product of static pressure and hydraulic diameter at a cross section (Eq. (6)) of the diverging microchannel. The effect of divergence can be noted from Fig. 15a that the Kn is approximately constant up to X/L = 0.4 owing to relatively constant product of pressure and hydraulic diameter. It can be accounted to the balancing of decrease in pressure with increase in hydraulic diameter up to X/L = 0.4. The hydraulic diameter is constant for $X/L > 0.8$ (Fig. 15a). The Kn indicates larger gradient for X/L = 0.8. The rarefied gas flow through diverging microchannel passes through three different flow behaviors, as depicted in Fig. 15b. The diverging microchannel can be divided approximately in three different zones to understand the physical aspects of the flow behavior as follows:
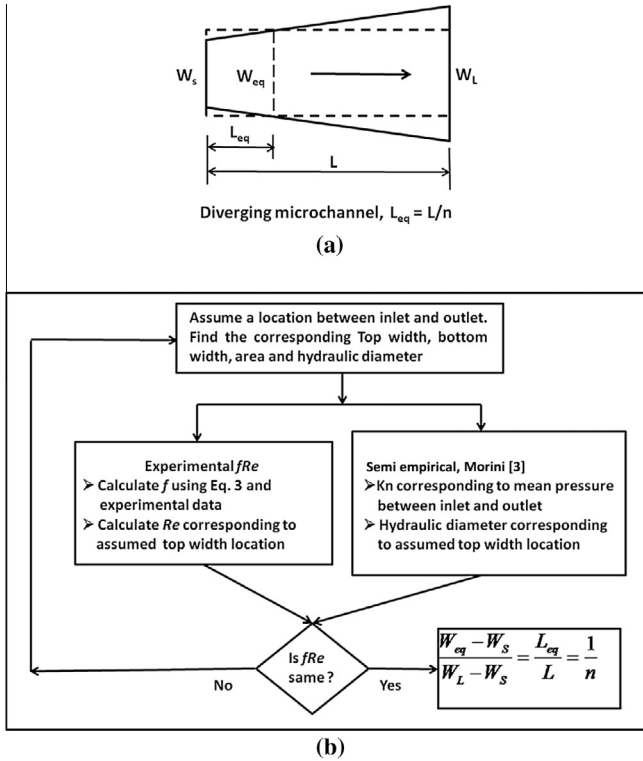
Fig. 14. (a) Concept of equivalent hydraulic diameter for diverging microchannel (W_S = top smaller width, W_L = top larger width, L = microchannel length, W_{eq} = equivalent top width, L_{eq} = length from inlet to equivalent top width location) and (b) Algorithm for obtaining location of equivalent hydraulic diameter.

Table 7
Static pressure drop for constant equivalent hydraulic diameter.

Microchannel geometry (trapezoidal cross section, D_h = 140 μm, L = 20 mm)	Static pressure drop (Pa)	% deviation with reference to uniform cross section
4° diverging	4011	6.96
8° diverging	3987	6.32
12° diverging	3963	5.68
16° diverging	3944	5.17
Uniform cross section	3750	–

Equivalent hydraulic diameter (D_h) for all the microchannels is maintained at 1/12.5 of microchannel length from inlet section. The mass flow rate 1.87×10^{-8} kg/s and Kn_o = 0.10 for all the four cases.

(i) *Zone I (X/L < 0.4), Nonlinear static pressure variation with flow deceleration* – The nonlinear pressure variation is attributed to two opposing effects: gas expansion, which increases with an increase in the divergence angle; and flow deceleration, due to increase in cross-sectional area (Figs. 9 and 13). The rate of deceleration is a function of gas expansion driven by the diverging cross section. The maximum pressure drop (approximately 70% of the overall pressure drop) occurs in this region (Fig. 8a) of the diverging microchannel due to larger shear stresses.

(ii) *Zone II (0.4 < X/L < 0.8), Linear pressure variation with constant velocity* – It is similar to incompressible flow behavior owing to balancing of viscous force by pressure force (Fig. 13). In this region, wall shear stress is nearly constant due to constant velocity. The rate of increase in velocity due to expansion is almost exactly balanced by a decrease in velocity brought about by an increase in cross-sectional area.

(iii) *Zone III (X/L > 0.8), Nonlinear static pressure variation with flow acceleration* – The existence of this zone can be noted clearly in case of 4° microchannel for centerline velocity variation (Fig. 9) and wall shear stress variation (Fig. 12b). The flow acceleration in zone III can be attributed to the sudden expansion downstream (channel outlet to reservoir) with expansion ratio of 4.3 for 4°, 1.3 for 16° channel. The sudden increase in cross section initiates gas expansion upstream away from the junction and continues with nonlinear pressure variation up to the junction [28]. The marginal flow acceleration can be noted in these cases (Fig. 9) due to lower sudden expansion ratio for 8°, 12° and 16° microchannels.

The existence of three different zones with microscale/rarefied gas flow suggests that the slip flow through diverging microchannel is significantly different than its continuum counterpart.

6.3. Absence of flow reversal

The absence of flow separation is noted on the basis of velocity distribution (Fig. 11) in the case of rarefied gas flow through 16° diverging channel; which is unlike liquid flow at conventional scale [43] and microscale [19]. This difference in liquid and gas flows through diverging microchannel can be attributed to the effect of slip/no slip at the wall and the magnitudes of kinetic energy and momentum diffusivity.

The kinetic energy of slip flow is negligible as compared to the driving pressure energy of the flow [28,30]. Therefore, any change in the kinetic energy due to a sudden change in the cross-section cannot influence the pressure gradient; and the flow separation is arrested. Hence, flow separation is absent in the present case of slip flow; whereas in case of liquid flow, Duryodhan et al. [19] observed flow separation downstream of the microchannel inlet.

Further, in the case of rarefied gas flow, the momentum diffusivity increases to a very large extent due to rarefaction as compared to continuum flow [28]. The larger momentum diffusivity causes the gas molecules to closely follow the surface just downstream of the microchannel inlet, unlike incompressible flow. These effects along with a larger slip downstream of the microchannel inlet (Fig. 12b) suppresses the flow separation altogether in case of slip flow through diverging microchannel.

6.4. Non-dimensional pressure drop and friction constant variation

The pressure drop for diverging microchannel can be non-dimensionalized with dynamic pressure at the microchannel inlet as follows:

$$K = \frac{\Delta P}{\frac{1}{2}\rho_i U_i^2} \tag{11}$$

where ΔP = pressure drop, Pa; ρ_i = density of gas at channel inlet, kg/m^3; U_i = average velocity at channel inlet, m/s. The non-dimensional pressure drop K is plotted in Fig. 16. The following correlations are proposed for K on the basis of experimental data points for 4°, 8°, 12° and 16° diverging microchannels.

$$K = \frac{358(1 + Kn_o)}{(\tan\theta)^{0.50}Re_i^{0.75}}$$
$$(4° \leqslant \theta \leqslant 16°, 0.004 < Kn_o < 0.02, 128 < Re_i < 1280) \tag{12}$$

$$K = \frac{708(1 + Kn_o)}{(\tan\theta)^{0.66}Re_i^{0.94}}$$
$$(4° \leqslant \theta \leqslant 16°, 0.02 < Kn_o < 0.10, 6.3 < Re_i < 128) \tag{13}$$

Fig. 16. Variation in experimental $K(Re_i)^a$ with Kn_o for diverging microchannel (mean hydraulic diameter D_h = 147 μm, length L = 20 mm, θ = full diverging angle, Reynolds number at channel inlet Re_i = 6.3–1280, Knudsen number at channel outlet Kn_o = 0.004–0.10, Mach number at channel inlet M_i = 0.04–0.45).
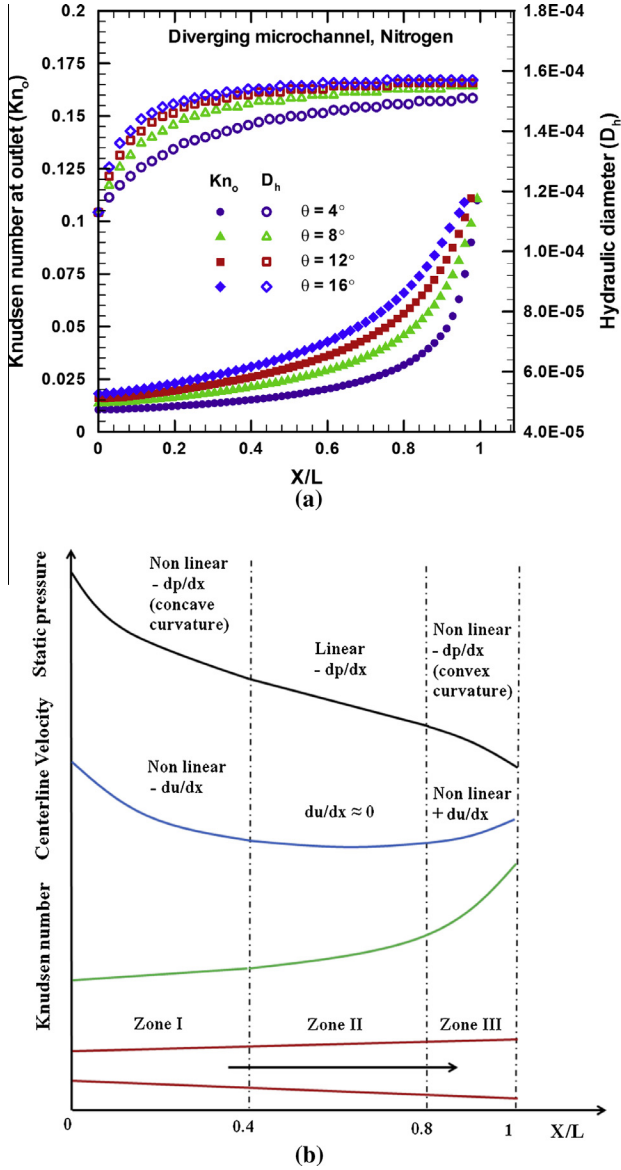

Fig. 15. (a) Effect of divergence on rarefaction (N–S solution) and (b) schematic diagram of low Mach number slip flow behavior through diverging microchannel.

Eq. (12) fits the experimental data points within ±13% range with a RMS error of 3.6% whereas Eq. (13) fits the experimental data points within ±15% range with a RMS error of 1.5%. The limited measurement resolution may be the reason for the relatively large error.

Fig. 16 shows the variation in $K(Re_i)^{0.94}$ with Kn_o. The correlation for $Kn_o > 0.02$ (Eq. (13)) indicates that the non-dimensional pressure drop increases with an increase in the divergence angle, whereas it is independent of Kn for larger Knudsen number. The correlation for $Kn_o < 0.02$ indicates that the pressure drop increases with decrease in Knudsen number. This result is in line with the variation in fRe (Fig. 4), noted earlier in Section 3.2.

An empirical correlation of experimental data for fRe is proposed in Eq. (14) for 4°, 8°, 12° and 16° diverging microchannels.

$$fRe(Kn_o, \theta) = \frac{C_1(\theta)}{1 + C_2(\theta)e^{-C_3(\theta)Kn_o}} \quad (4° \leqslant \theta \leqslant 16°, 0.004 < Kn_o$$
$$< 0.10, 6.3 < Re_i < 1280) \tag{14}$$

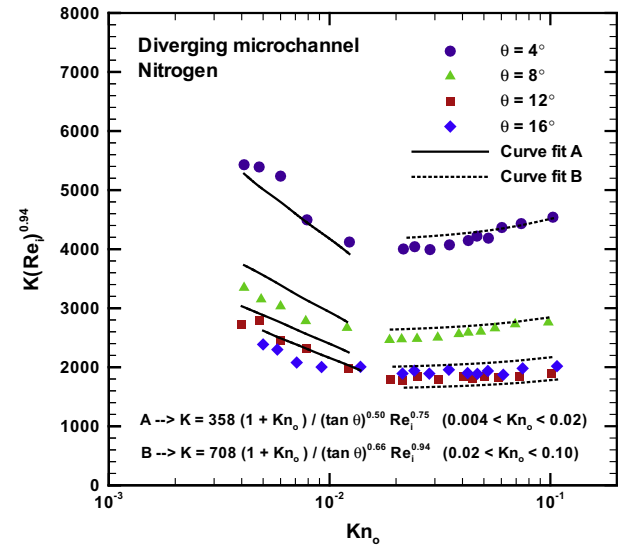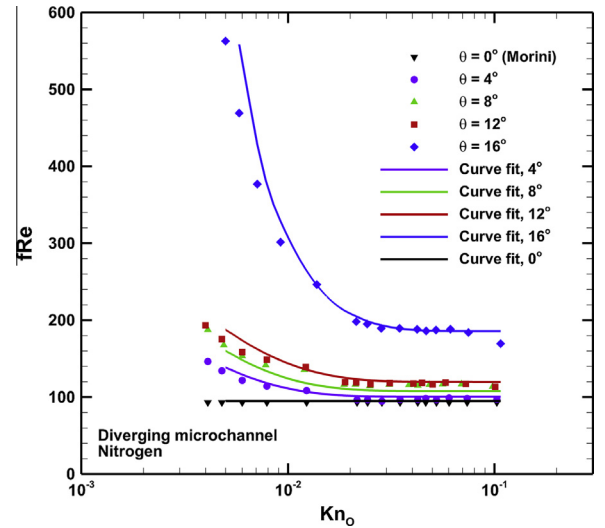where C_1, C_2 and C_3 in Eq. (14) are introduced as following (θ in Eq. (12) is in degrees).

Fig. 17. Variation in experimental fRe with Kn_o for diverging microchannel (mean hydraulic diameter D_h = 147 μm, length L = 20 mm, θ = full diverging angle, Reynolds number at channel inlet Re_i = 6.3–1280, Knudsen number at channel outlet Kn_o = 0.004–0.10, Mach number at inlet M_i = 0.04–0.45).

$$C_1(\theta) = \frac{94.86 - 5.36\theta}{1 - 0.07\theta + 0.00066\theta^2} \tag{15}$$

$$C_2(\theta) = 0.002 - 0.346\theta + 0.045\theta^2 - 0.0018\theta^3 \tag{16}$$

$$C_3(\theta) = 235.78 - 6.85\theta \tag{17}$$

Fig. 17 shows the variation in fRe with Kn_o. The estimated values from Eq. (14) recover the values obtained using correlation proposed by Morini [3] for uniform microchannel (Eq. (7)).

6.5. Non-dimensional mass flow rate variation

The mass flow rate for diverging microchannel is non-dimensionalized with non-dimensionalization proposed by Shen et al. [44] for microchannels as follows:
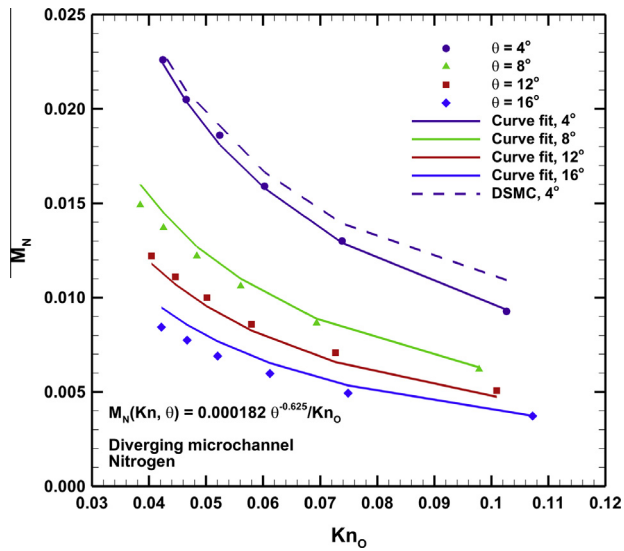
Fig. 18. Variation in experimental M_N with Kn_o for diverging microchannel (mean hydraulic diameter $D_h = 147$ μm, length $L = 20$ mm, θ = full diverging angle, Reynolds number at channel inlet $Re_i = 6.3$–1280, Knudsen number at channel outlet $Kn_o = 0.004$–0.10, Mach number at inlet $M_i = 0.04$–0.45).

$$M_N = \frac{\dot{M}_{exp}}{\frac{1}{2}(\rho_i + \rho_o)A_o v_m} \qquad (18)$$

where $\dot{M}_{exp}$ = measured mass flow rate (kg/s), ρ_i, ρ_o = density at channel inlet and outlet, respectively, (kg/m^3), A_o = cross-sectional area at the channel outlet (m^2), and $v_m = \sqrt{2RT}$ is the most probable molecular speed (m/s). The non-dimensional mass flow rate M_N is plotted in Fig. 18. The following correlation is proposed for M_N on the basis of experimental data points for 4°, 8°, 12° and 16° diverging microchannels.

$$M_N = \frac{0.00018\theta^{-0.625}}{Kn_o} \quad (4° \leqslant \theta \leqslant 16°, 0.04 < Kn_o < 0.10, 6.3$$
$$< Re_i < 1280) \qquad (19)$$

where θ is in radians. The nonlinear M_N curve fit relation is obtained with an r^2 value of 99% using experimental data sets. Eq. (19) fits the experimental data points within ±12% range with a RMS error of 0.05%. The variation in correlation for M_N with Kn_o is plotted in Fig. 18. The correlation for M_N (Eq. (19)) indicates that the non-dimensional mass flow rate decreases with an increase in the divergence angle and the Knudsen number.

7. Conclusions

Experiments are performed for nitrogen flowing through different diverging microchannels of divergence angle (4°, 8°, 12° and 16°), hydraulic diameter (118, 147 and 177 μm) and length (10, 20 and 30 mm) in the continuum and slip flow regimes (0.0005 < Kn < 0.10; 0.4 < Re < 1280). The static pressure drop is measured between the inlet and outlet ports of the microchannels and analyzed in detail. The local flow behavior is investigated on the basis of numerical analysis of local static pressure variation, velocity distribution, wall shear stress and force balance. Both Navier–Stokes based calculations and Direct Simulation Monte Carlo techniques have been employed for conducting the numerical simulations.

The proportion of viscous pressure drop with reference to total pressure drop indicates that the viscous force dominates for low Mach number slip flow through a diverging microchannel. The velocity distribution shows absence of flow reversal in the diverg-

ing microchannel owing to slip at the wall, larger viscous diffusion, and lower kinetic energy in diverging microchannel. The numerical results indicate three distinct zones with different flow behavior in a diverging microchannel. Zone I indicates rapid flow deceleration and decrease in wall shear stress due to gas expansion owing to diverging geometry. It indicates maximum pressure drop with reference to the overall pressure drop due to relatively large inertia and shear stresses. Further downstream, uniform centerline velocity and uniform wall shear stress are noted in zone II due to balancing of pressure force with shear force. Zone III exhibits flow acceleration with increase in wall shear stress due to sudden expansion downstream of the channel. The overall pressure drop decreases with an increase in divergence angle due to larger pressure recovery (as a result of larger rate of deceleration) in larger divergence angle microchannel.

The concept of equivalent hydraulic diameter is proposed; the equivalent hydraulic diameter is calculated for the entire experimental dataset. The calculation of equivalent hydraulic diameter indicates that location of the characteristic length for diverging microchannel approaches the microchannel inlet section with increasing rarefaction. Empirical relations for the mass flow rate and Poiseuille number are suggested. The former shows that mass flow in divergent channels depends inversely on Kn number within the slip regime. The later relation is a universal one which recovers the well-known correlation for the limiting case of a straight microchannel at $\theta = 0°$.

These experimental and numerical findings on low Mach number slip flow through diverging microchannels are considerably different from its continuum counterpart. It should prove a valuable contribution in the literature on the studies of rarefied gas flow through diverging microchannels and should help to improve our understanding of gas flow through complex microchannels.

References

[1] Weng CI, Li WL, Hwang CC. Gaseous flow in microtubes at arbitrary Knudsen numbers. Nanotechnology 1999;10:373–9.
[2] Zohar Y, Lee SYK, Lee WY, Jiang L, Tong P. Subsonic gas flow in a straight and uniform microchannel. J Fluid Mech 2002;472:125–51.
[3] Morini GL. Laminar liquid flow through silicon microchannels. J Fluids Eng 2004;126:485–9.
[4] Agrawal A, Agrawal A. Three-dimensional simulation of gaseous slip flow in different aspect ratio microducts. Phys Fluids 2006;18:103604-1–103604-11.
[5] Dongari N, Agrawal A, Agrawal A. Analytical solution of gaseous slip flow in long microchannels. Int J Heat Mass Transfer 2007;50:3411–21.
[6] Ewart T, Perrier P, Graur IA, Meolans JG. Mass flow rate measurements in a microchannel, from hydrodynamic to near free molecular regimes. J Fluid Mech 2007;584:337–56.
[7] Roohi E, Darbandi M. Extending the Navier–Stokes solutions to transition regime in two-dimensional micro and nanochannel flows using information preservation scheme. Phys Fluids 2009;21:082001-1–082001-12.
[8] Verma B, Demsis A, Agrawal A, Prabhu SV. Semiempirical correlation for the friction factor of gas flowing through smooth microtubes. J Vac Sci Technol A 2009;27(3):584–90.
[9] Vijayalakshmi K, Anoop KB, Patel HE, Harikrishna PV, Sundararajan T, Das SK. Effects of compressibility and transition to turbulence on flow through microchannels. Int J Heat Mass Transfer 2009;52:2196–204.
[10] Pitakarnnop J, Varoutis S, Valougeorgis D, Geoffroy S, Baldas L, Colin S. A novel experimental setup for gas microflows. Microfluid Nanofluid 2010;8:57–72.
[11] Singh N, Agrawal A. The Burnett equation in cylindrical coordinates and its solution for flow in a microtube. J Fluid Mech 2014. to appear.
[12] Singh N, Dongari N, Agrawal A. Analytical solution of plane Poiseuille flow within Burnett hydrodynamics. Microfluid Nanofluid 2014;16:403–12.
[13] Sreekanth AK. Slip flow through long circular tubes. In: Trilling L, Wachman HY, editors. Proceedings of the sixth international symposium on rarefied gas dynamics. Academic Press; 1969. p. 667–80.

[14] Demsis A, Verma B, Prabhu SV, Agrawal A. Experimental determination of heat transfer coefficient in the slip regime and its anomalously low value. Phys Rev E 2009;80:016311.

[15] Demsis A, Prabhu SV, Agrawal A. Influence of wall condition on friction factor for flow of gases under slip condition. Exp Thermal Fluid Sci 2010;34(8):1448–55.

[16] Agrawal A. A comprehensive review of gas flow in microchannels. Int J Micro-Nanoscale Transp 2011;2(1).

[17] Pan CT, Chuang HS, Cheng CY, Yang CT. Micro-flow measurement with a laser diode micro-particle image velocimetry. Sens Actuators A 2004;116:51–8.

[18] Tsai CH, Chen HT, Wang YN, Lin CH, Fu LM. Capabilities and limitations of 2-dimensional and 3-dimensional numerical methods in modeling the fluid flow in sudden expansion microchannels. Microfluid Nanofluid 2007;3:13–8.

[19] Duryodhan VS, Singh SG, Agrawal A. Liquid flow through a diverging microchannel. Microfluid Nanofluid 2012;14:53–67.

[20] Abdelall FF, Hahn G, Ghiaasiaan SM, Abdel-Khalik SI, Jeter SS, Yoda M, et al. Pressure drop caused by abrupt flow area changes in small channels. Exp Thermal Fluid Sci 2005;29:425–34.

[21] Stemme E, Stemme G. A valveless diffuser/nozzle-based fluid pump. Sens Actuators A 1993;39:159–67.

[22] Olsson A, Stemme G, Stemme E. A valves-less planar fluid pump with two pump chambers. Sens Actuators A 1995;46–47:549–56.

[23] Gerlach T. Microdiffusers as dynamic passive valves for micropump applications. Sens Actuators A 1998;69:181–91.

[24] Singhal V, Garimella SV, Murthy JY. Low Reynolds number flow through nozzle-diffuser elements in valveless micropumps. Sens Actuators A 2004;113:226–35.

[25] Wang YC, Hsu JC, Chen HY, Kuo PC, Lee YC. Loss characteristics and flow rectification property of diffuser valves for micropump applications. Int J Heat Mass Transfer 2009;52:328–36.

[26] Akbari M, Sinton D, Bahrami M. Laminar fully developed flow in periodically converging diverging microtubes. Heat Transfer Eng 2010;31(8):628–34.

[27] Rathakrishnan E, Sreekanth AK. Rarefied flow through sudden enlargements. Fluid Dyn Res 1995;16:131–45.

[28] Varade VV, Agrawal A, Pradeep AM. Behavior of rarefied gas flow near junction of a suddenly expanding tube. J Fluid Mech 2014;739:363–91.

[29] Agrawal A, Djenidi L, Antonia RA. Simulation of gas flow in microchannels with a sudden expansion or contraction. J Fluid Mech 2005;530:135–44.

[30] Lee WY, Wong M, Zohar Y. Microchannels in series connected via a contraction/expansion section. J Fluid Mech 2002;459:187–206.

[31] Lee PC, Pan C. Boiling heat transfer and two-phase flow of water in a single shallow microchannel with a uniform or diverging cross section. J Micromech Microeng 2008;18:025005.

[32] Wu P, Little WA. Measurement of friction factors for the flow of gases in very fine channels used for microminiature Joule–Thomson refrigerators. Cryogenics 1983;23:273–7.

[33] Fluent 6.3.26, 3ddp, 2006.

[34] Harley J, Huang Y, Bau H, Zemel JN. Gas flow in microchannels. J Fluid Mech 1995;284:257–74.

[35] Arkilic EB, Schimidt MA, Breuer KS. Gaseous slip flow in long micro-channels. J Microelectromech Syst 1997;6:167–78.

[36] Morini GL, Spiga M. Slip flow in rectangular microtube. Microscale Thermopys Eng 1998;2:273–82.

[37] Agrawal A, Prabhu SV. Survey on measurement of tangential momentum accommodation coefficient. J Vac Sci Technol A 2008;26:634–45.

[38] OpenFOAM 2.3.0 User Guide, 2014.

[39] Bird G. Monte Carlo simulation of gas flows. Annu Rev Fluid Mech 1978;10(1):11–31.

[40] Scanlon T, Roohi E, White C, Darbandi M, Reese JM. An open source, parallel DSMC code for rarefied gas flows in arbitrary geometries. Comput Fluids 2010;39(10):2078–89.

[41] Darbandi M, Roohi E. Applying a hybrid DSMC/Navier–Stokes frame to explore the effect of splitter catalyst plates in micro/nano propulsion systems. Sens Actuators A 2013;189:409–19.

[42] Roohi E, Darbandi M. Recommendations on performance of parallel DSMC algorithm in solving subsonic nanoflows. Appl Math Model 2012;36(5):2314–21.

[43] White FM. Fluid mechanics. 6th ed. New York: The McGraw-Hill Companies; 2008. p. 389–402.

[44] Shen C, Fan J, Xie C. Statistical simulation of rarefied gas flows in micro-channels. J Comput Phys 2003;189(2):512–26.

[45] Varade VV, Agrawal A, Pradeep AM. Experimental study of rarefied gas flow near sudden contraction junction of a tube. Phys Fluids 2014;26:062002. http://dx.doi.org/10.1063/1.4881940.

[46] Varade VV, Agrawal A, Pradeep AM. Slip flow through converging microchannel: experiments and three-dimensional simulations. J Micromech Microeng 2015. to appear.